

Study of Rhamnose Radicals in the Solid State Adopting a Density Functional Theory Cluster Approach

Ewald Pauwels,* Veronique Van Speybroeck, and Michel Waroquier

Center for Molecular Modeling, Ghent University, Proeftuinstraat 86, B-9000 Gent, Belgium

Received: January 11, 2006; In Final Form: March 16, 2006

A theoretical study is performed on the radiation-induced radicals in crystalline α -L-rhamnose, using density functional theory (DFT) calculations. Irrespective of earlier structural assignments, a host of possible radical models is examined in search for a structure that accurately reproduces experimental electron paramagnetic resonance (EPR) properties. A cluster approach is followed, incorporating all hydrogen bond interactions between radical and crystalline environment. Hyperfine coupling tensors as well as g tensors are determined and a comparison is made with available experimental data. Three carbon-centered hydroxyalkyl radicals are validated, in accordance with experimental suggestions for their structure. The occurrence of a carbon-centered oxygen anion radical for one of the radical species is rejected on theoretical grounds, and instead an altered hydroxyalkyl structure is suggested. Our cluster calculations are able to determine g and hyperfine tensors for the oxygen-centered alkoxy radical in rhamnose, in accordance with one of the two measurements for this species. For all radical models, quantitative agreement with experimental hyperfine tensors is obtained by performing full cluster DFT calculations. The inclusion of the molecular environment for the determination of this EPR property proved to be essential.

1. Introduction

Radiation-induced radicals in solid-state sugars have been the subject of many studies, from both an experimental and theoretical point of view. As carbohydrates are extremely abundant in plants and animals, these compounds are potential probes in detecting irradiation of various foodstuffs. The search for a practical radiation dosimeter that allows identification as well as reliable dose estimates has attracted much interest,¹ in particular due to the increasing use of industrial treatments with ionizing radiation to improve the hygienic quality and shelf life of foodstuffs. Due to the relative longevity of radiation-induced radicals in sugars, they can present a suitable probe to determine the radiation dose,² which is most easily determined with the aid of electron paramagnetic resonance (EPR) spectroscopy.³

On a more fundamental level, EPR (or a derived technique) can be used to examine the radiation chemistry that governs the eventual radical formation in sugars. In this way, several studies have identified the radiation-induced radicals in single crystals of various carbohydrates, such as glucose,⁴ fructose,⁵ sorbose⁶ or sucrose.⁷ A clear insight in the radiation chemistry for these relatively simple compounds is valuable if more complex systems are to be understood. For instance, it has been shown that deoxyribose sugar radicals are involved in the radiation damage process leading up to strand breaks in DNA.⁸

From the latter perspective, the α -rhamnose sugar has constituted a model system for the investigation of primary radiation-induced events. It was one of the first crystalline carbohydrates in which trapped electrons⁹ were observed following low-temperature irradiation. These electrons are localized at intermolecular sites within the crystal matrix, stabilized by hydrogen bonds with hydroxyl groups from surrounding rhamnose molecules. The stability and geometrical

characteristics of these primary reduction products have been studied in detail.^{10–13} Another radiation-induced species that was observed is a primary oxidation product: an oxygen centered alkoxy radical. These radiation products are usually very unstable and can therefore only be observed after irradiation at low temperatures. Samskog and Lund¹⁴ observed a rhamnose alkoxy radical after irradiation at 77 K, whereas Budzinski and Box¹⁵ made measurements at 4.2 K, allowing a thorough characterization of complete g and hyperfine tensors. Interestingly, although g and hyperfine tensors were significantly differing in both studies, the measured signals were attributed to the same structure—a radiation product I_{exp} obtained by hydroxyl proton abstraction from oxygen O4. This structure is presented in Figure 1, along with an overview of all other radical models that were proposed. A summary of the measured g and hyperfine tensors is presented in Table 1. The results of Samskog and Lund are labeled by $I_{\text{exp,SL}}$ and those of Budzinski and Box by $I_{\text{exp,BB}}$. All principal directions of g and hyperfine tensors are specified by direction cosines with respect to the orthogonal (a^*bc) reference system.

It was first established by Samskog et al.^{12,13} that upon light exposure or thermal treatment, the trapped electrons in rhamnose easily decay to form hydroxyalkyl radicals. A definite structure for this relatively stable secondary reduction product was determined by Sagstuen et al.¹⁶ in an extensive study of irradiated rhamnose at different temperatures. Using a variety of EPR and ENDOR techniques, a C3-centered hydroxyalkyl radical II_{exp} was found after irradiation at 65 K and exposure to light. On gradually increasing the temperature above 110 K, one exchangeable proton coupling disappeared for the II_{exp} radical species. This was tentatively attributed to the loss of a hydroxyl proton, yielding a structure III_{exp} . Additionally, Sagstuen et al. identified other radicals in rhamnose irradiated at room temperature. One is a C2-centered hydroxyalkyl radical (structure IV_{exp} in Figure 1) and the other is obtained by

* To whom all correspondence should be addressed. Fax: 32 9 264 66 97. E-mail: ewald.pauwels@UGent.be.

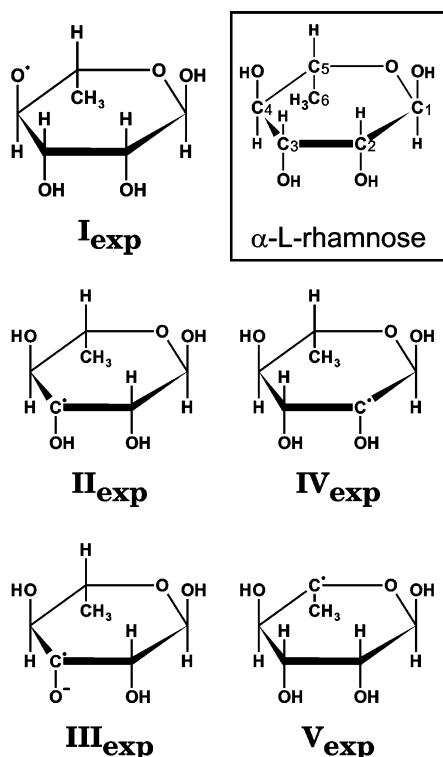


Figure 1. Atom numbering in α -L-rhamnose and overview of proposed radical structures as suggested from EPR experiments. Oxygens and hydrogens are numbered according to the carbon to which they are bound.

hydrogen abstraction at C5 (V_{exp}). The latter was found to rapidly decay. Indications were found that other room-temperature stable radicals are present, in much lower relative abundance.

However, some of the proposed radical models in rhamnose are only tentative and several ambiguities remain. The objective of this work is to assess the validity of these models by using computational methods based on density functional theory (DFT).¹⁷ More specifically, a host of possible structures is examined and their EPR spectroscopic properties (hyperfine and g tensors) are calculated in the search for a radical that reproduces the experimental signals. The usefulness and feasibility of such an approach based on DFT has been extensively demonstrated for several other sugars.¹⁸ However, in most studies a *single molecule* approach was followed, in which only the radical itself is taken up in the computational model. Such a method effectively models the radical in a vacuum and therefore presents a very crude approximation for a radical that is otherwise embedded within a crystal lattice. An improved description of the solid state is offered by the *cluster* approach. In this model space, a part of the crystal lattice is explicitly modeled by placing discrete molecules around the target radical, in accordance with the crystal structure. The model space then consists of a central radical surrounded by several neighboring molecules from the lattice and hence can explicitly account for intermolecular interactions between the radical and these additional molecules. Despite the substantially larger computational cost that is associated with cluster models, it has been established that they offer a superior description of radical geometries within organic crystals.^{19,20} In addition, it was verified in a recent study by the authors²¹ that EPR properties calculated with full inclusion of the cluster model are in significantly better agreement with experiment. For these reasons, a cluster approach was adopted for all calculations in the present work.

TABLE 1: Summary of EPR and ENDOR Measurements on rhamnose

signal	$A_{\text{iso}}/g_{\text{iso}}$	$A_{\text{aniso}}/g_{\text{aniso}}$	direction cosines vs $\langle a^*bc \rangle$		
$I_{\text{exp,SL}} (77 \text{ K})^a$					
$I_{\text{SL-1}}$	112.1				
$I_{\text{SL-2}}$	39.2				
$I_{\text{SL-g}}$	2.0184	2.0032	0.020	0.982	-0.189
		2.0064	-0.698	0.149	0.700
		2.0456	0.716	0.118	0.688
$I_{\text{exp,BB}} (4.2 \text{ K})^b$					
$I_{\text{BB-1}}$	-3.0	-7.7	0.127	0.003	0.991
		-7.3	0.990	0.056	-0.127
		15.1	-0.056	0.998	0.003
$I_{\text{BB-2}}$	5.2	-12.7	-0.129	0.167	0.927
		-0.2	0.787	0.616	-0.001
		12.9	-0.620	0.760	-0.212
$I_{\text{BB-3}}$	0.1	-5.9	-0.023	0.221	0.974
		-4.9	0.364	0.909	-0.197
		10.8	0.930	-0.351	0.102
$I_{\text{BB-4}}$	5.2	-7.8	0.259	-0.079	0.962
		-0.1	0.744	0.651	-0.146
		7.9	-0.050	0.754	0.228
$I_{\text{BB-5}}$	67.2	-4.0	0.743	-0.481	-0.464
		-0.2	0.409	-0.220	0.865
		8.3	0.528	0.848	-0.033
$I_{\text{BB-6}}$	53.9	-7.7	0.219	0.687	0.691
		-2.0	0.377	-0.594	0.710
		9.7	0.899	-0.417	0.129
$I_{\text{BB-7}}$	3.9	-1.9	0.696	-0.607	0.381
		-0.7	0.584	0.789	0.189
		2.6	-0.416	0.091	0.904
$I_{\text{BB-g}}$	2.0096	2.0018	-0.339	-0.691	0.637
		2.0068	-0.554	0.694	0.458
		2.0202	-0.759	-0.198	-0.619
$II_{\text{exp}} (65 \text{ K})^c$					
$II-1$	92.5–100.9				
$II-2$	16.8–19.6				
$II-3$	16.8–19.6				
$III_{\text{exp}} (+120 \text{ K})^c$					
$III-1$	96.1	-5.2	-0.276	0.380	0.883
		-1.4	-0.945	0.006	-0.322
		6.6	0.177	0.923	-0.342
$III-2$	16.8–19.6				
$III-g$	2.0039	2.0027	0.083	0.971	-0.223
		2.0038	-0.771	0.204	0.604
		2.0051	-0.632	-0.122	-0.766
$IV_{\text{exp}} (\text{RT})^c$					
$IV-1$	23.7	-6.4	-0.378	0.603	0.702
		-4.3	0.422	0.788	-0.449
		10.7	0.824	-0.127	0.553
$IV-2$	4.4	-6.3	0.814	-0.569	0.118
		-3.8	0.581	0.798	-0.161
		10.1	-0.002	0.200	0.980
$IV-3$	4.7	-10.2	0.798	0.586	0.143
		-9.1	0.329	-0.621	0.711
		19.3	-0.506	0.520	0.688
$IV-4$	-3.5	-4.0	-0.344	0.101	0.934
		-1.5	0.910	-0.210	0.358
		5.5	0.232	0.972	-0.020
$IV-g$	2.0030	2.0020	0.621	0.781	0.060
		2.0034	0.613	-0.533	0.583
		2.0036	-0.488	0.325	0.810
$V_{\text{exp}} (\text{RT})^c$					
$V-1$	95.3				
$V-2$	56.0				

^a Reference 14. ^b Reference 15. ^c Reference 16.

2. Computational Details

A cluster model of rhamnose molecules was constructed in accordance with the structure of the α -L-rhamnose monohydrate crystal as determined from neutron diffraction.²² The crystal structure is monoclinic, with space group symmetry $P2_1$ and

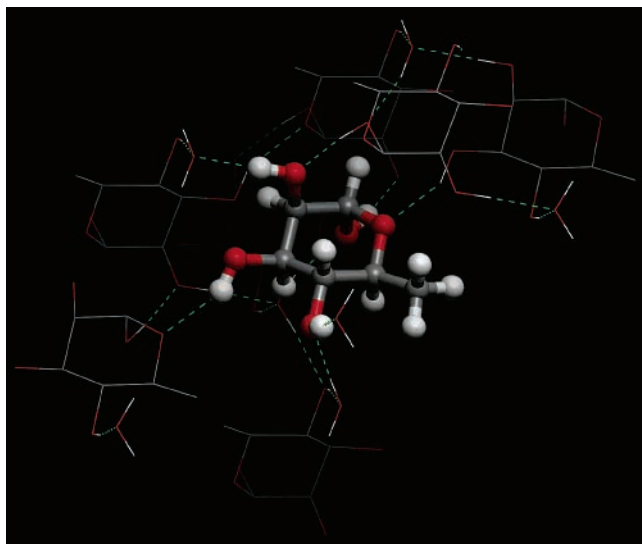


Figure 2. Central species in the employed cluster model is surrounded by seven α -L-rhamnose and eight water molecules. Some of the hydrogen atoms are not displayed to make the figure more transparent.

the unit cell contains two rhamnose and two water molecules. Starting from the complete lattice, a cluster was obtained by considering all molecules that are engaged in hydrogen bonds with a central rhamnose molecule. The resulting model space contains eight rhamnose and eight water molecules in total, as illustrated in Figure 2. Although this cluster already contains 208 atoms, it is in fact the smallest model that has any physical significance. Subsequently, initial geometries for the different radicals were created by removing hydrogen atoms from the central molecule. The radical structure was then optimized within the cluster in search for conformations with minimal energy. During all geometry optimizations, all “lattice” molecules surrounding the central defect were held fixed at their crystal positions.

The initial assessment of possible radical structures was performed employing a two-layered ONIOM²³ approach of the cluster system. In this scheme, the central radical is treated at the DFT-B3LYP level of theory²⁴ with a 6-311G** basis set,²⁵ whereas the surrounding rhamnose (7) and water molecules (8) are described with the aid of the semiempirical PM3 Hamiltonian.²⁶ Subsequently, EPR parameters were calculated for the optimized central radical geometry only. This is effectively a single molecule EPR calculation, but it allows a fast and qualitative analysis of the spectroscopic properties. We will refer to this methodology with the B3LYP-PM3-8/B3LYP-1 shorthand.

Based on the results of these calculations, a further selection was made of suitable radicals. These structures were then re-optimized, in which both the radical and the cluster environment were treated at the B3LYP level with a 6-311G** basis. These optimizations, encompassing eight rhamnose species and eight H₂O molecules, are high-level calculations and impose a considerable burden on computational resources, as the entire system is treated *ab initio*. The ensuing determination of the hyperfine coupling tensors was performed at the same level of theory, again for the entire cluster. Hence, we will maintain the B3LYP-8/B3LYP-8 shorthand for this method. Unfortunately, this methodology proved too expensive from a computational point of view for the calculation of *g* tensors and these properties were obtained from single molecule EPR calculations of the optimized radical structure only (referred to as the B3LYP-8/B3LYP-1 scheme).

3. Initial Assessment of Possible Radical Structures

Starting from the undamaged rhamnose, fourteen trial models were initially proposed, independent of any radical structure that was suggested on the basis of the EPR experiments. Such a procedure ensures an unbiased evaluation of the different radical models on their ability to reproduce the experimental EPR measurements. However, all models were created in the assumption that the pyranose ring is not broken in any of the radiation-induced products of rhamnose. Even though open-ring radicals have been reported in other sugars (see, e.g., ref 27), they will not be considered in this work.

In a first set of calculations, all possible radicals due to homolytic cleavage of a C–H bond were examined. These models, labeled R_{C1} to R_{C6} in Figure 3, are generated by abstracting a hydrogen atom from carbons C1–C6, respectively. The calculated isotropic and anisotropic hyperfine and *g* tensor values, resulting from B3LYP-PM3-8 geometry optimization and consequent single molecule EPR calculations, are also listed in Figure 3. Negligible hyperfine couplings from other atoms in the radical model were left out and corresponding eigenvectors are supplied in the Supporting Information (SI-1). It is obvious that R_{C1} to R_{C6} can only be viable models for the carbon-centered II_{exp}, III_{exp}, IV_{exp} or V_{exp} paramagnetic species. Such radicals are characterized by rather isotropic *g* tensors ($g_{\text{aniso1}} \approx g_{\text{aniso2}} \approx g_{\text{aniso3}}$), which can be easily verified in both the measurements of Table 1 and the calculated data in Figure 3. As a result, this spectroscopic property does not present a suitable tool to discriminate between radical models for carbon-centered species, because all *g* tensors are too similar. The hyperfine tensors, on the other hand, are much more sensitive to local, geometrical differences and we will mainly rely on these EPR parameters to evaluate the different carbon-centered models.

(i) Species V_{exp} was characterized by Sagstuen et al.¹⁶ to display one large hyperfine splitting of about 95 MHz and a quartet splitting around 56 MHz (Table 1). The latter feature reveals that three β -protons have a nearly equivalent hyperfine interaction. In accordance with the structure suggested by Sagstuen et al., radical model R_{C5} is the only viable candidate. At temperatures above 0 K, the three methyl protons (H6a, H6b, H6c) are subject to a thermal rotational movement, averaging out their hyperfine interactions. Because temperature was not taken into account for the simulations in this work, the methyl group is “frozen” at the orientation with minimal energy in which H6a to H6c give rise to individual coupling tensors (taken up in Figure 3). A rough estimate for the effect of the rotational motion on the isotropic hyperfine value is obtained by averaging over the distinct contributions. The resulting H6avg of 51.2 MHz is very close to the 56 MHz in species V_{exp}. Proton H4, which is also in a β -position with respect to the main locus of the unpaired electron, has an isotropic value of 89 MHz, in accordance with the 95 MHz of feature V-1 in Table 1.

(ii) Only one minor feature stands out in radical species IV_{exp}: a relatively small hyperfine coupling of some 20 MHz. Other hyperfine tensors were determined in the experiments by Sagstuen et al.,¹⁶ but the corresponding isotropic values are very small (all below 10 MHz in absolute value). Because the initial assessment of radical structures relies on calculations at a moderate level of theory (B3LYP-PM3-8/B3LYP-1), some caution is recommended when making an assignment based mainly on isotropic hyperfine couplings. This parameter in particular can, to some degree, alter in high-level geometry optimizations and/or EPR calculations, as it is very sensitive to local, structural or electronic effects (see, e.g., ref 20). Hence,

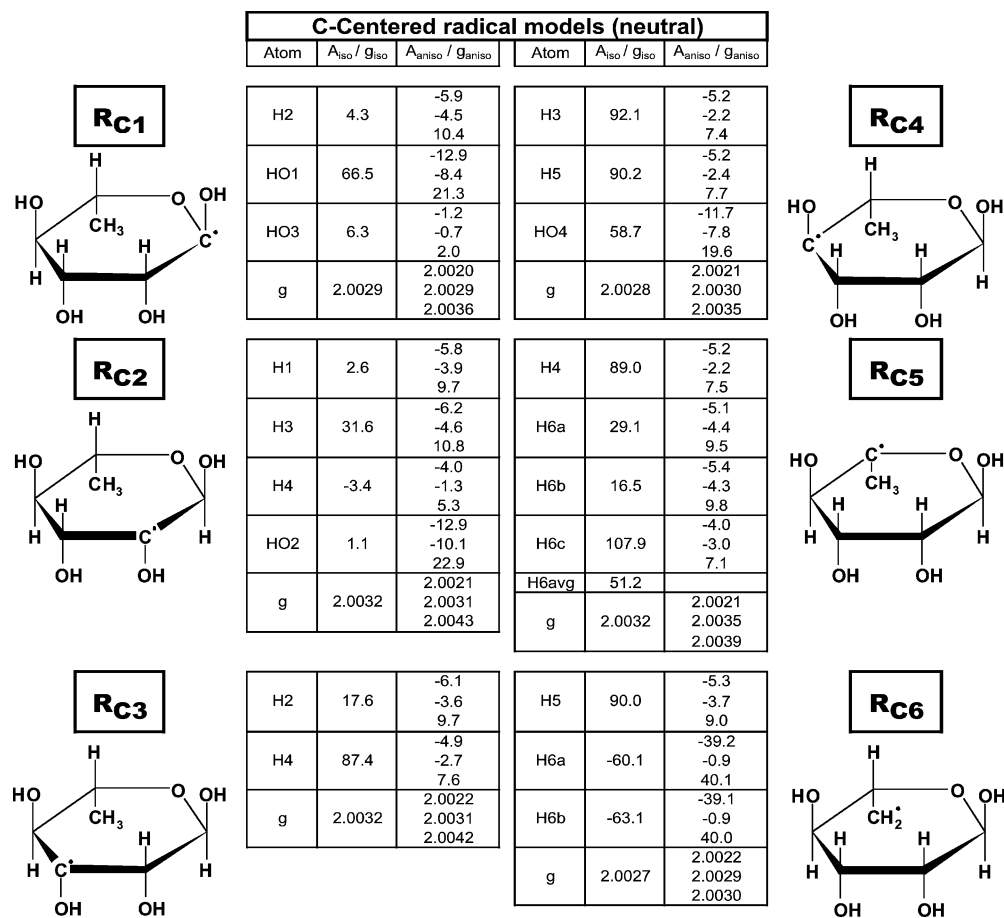


Figure 3. Overview of calculated g and hyperfine tensor values for various carbon-centered radical models, obtained at the B3LYP-PM3-8/B3LYP-1 level of theory. Hyperfine values are reported in megahertz.

radical models R_{C1} and R_{C2} can be considered as possible candidates for the IV_{exp} species. Both are characterized by a single hyperfine coupling of moderate intensity and several other very weak hyperfine couplings. Although R_{C2} is in better quantitative agreement with the experimental EPR data, R_{C1} cannot be excluded based solely on the isotropic hyperfine value. Closer examination of the anisotropic couplings, however, reveals that the HO1 tensor of R_{C1} is incompatible with the experimental IV-1 tensor. Model R_{C2} , on the other hand, closely reproduces the anisotropic eigenvalues of about -6 , -4 and $+10$ MHz. Additionally, the principal axes (given in the Supporting Information SI-1) give further support for the assignment of the R_{C2} structure to the IV_{exp} radical species.

(iii) The hyperfine data for species II_{exp} and III_{exp} , as determined in ref 16, are virtually identical. In fact, the former species was found to be transformed into the latter upon gradual warming of the sample, resulting in the disappearance of a minor, exchangeable proton coupling in the EPR spectrum. Both species have one large (around 95 MHz) and a much smaller 18 MHz coupling in common, whereas II_{exp} is characterized by an additional 18 MHz splitting. Examining the remaining radical models, it is found that the R_{C3} structure is in close agreement with the EPR data of both II_{exp} and III_{exp} . R_{C4} with two large 90 MHz couplings is not a viable candidate and so are R_{C5} and R_{C6} . Radical model R_{C1} could be considered, as it has one large and two smaller isotropic splittings. However, the anisotropy of the HO1 tensor differs from the characteristic III-1 principal components in the experiment. For model R_{C3} , both isotropic and anisotropic hyperfine values are already in close quantitative agreement with the III_{exp} EPR data, but the model lacks one hyperfine coupling to entirely reproduce the II_{exp} measurements.

As will be shown further on, this residual splitting can only be found by performing calculations at a higher level of theory. Therefore, we retain R_{C3} as a suitable model structure for both the II_{exp} and III_{exp} radical species.

To some degree, this is in accordance with the assignments by Sagstuen et al. who suggested the same structure on the basis of the II_{exp} EPR measurements. However, the disappearing exchangeable proton in III_{exp} was tentatively attributed to the loss of a hydroxyl proton, resulting in the formation of a carbon-centered oxygen anion radical (structure III_{exp} in Figure 1). To examine this possibility, we investigated four additional models (presented in Figure 4), obtained by removing a hydroxyl proton from radical models R_{C1} to R_{C4} . Geometry optimization and EPR calculation on these radical anions R_{CO1} to R_{CO4} , employing the B3LYP-PM3-8/B3LYP-1 procedure, result in the spectroscopic properties listed in Figure 4.

The calculated g tensors for these structures are in better accordance with experiment. They are somewhat more anisotropic than the g tensors in Figure 3 and the principal components now closely match the measured values. However, the hyperfine coupling pattern for any of the proposed radical anions completely disagrees with the experimental observations for III_{exp} . Whereas both R_{CO3} and R_{CO4} only give rise to two similar, intermediate coupling constants, the hyperfine splittings in models R_{CO1} and R_{CO2} never exceed 20 MHz. In addition, the principal directions for any of the calculated hyperfine tensors (provided as Supporting Information SI-2) do not correspond with the experimental III-1 tensor axes. Yet, this spectroscopic parameter can be regarded as a sensitive probe for the validity of the proposed radical model because it does not depend as much on the level of theory. Hence, on the basis

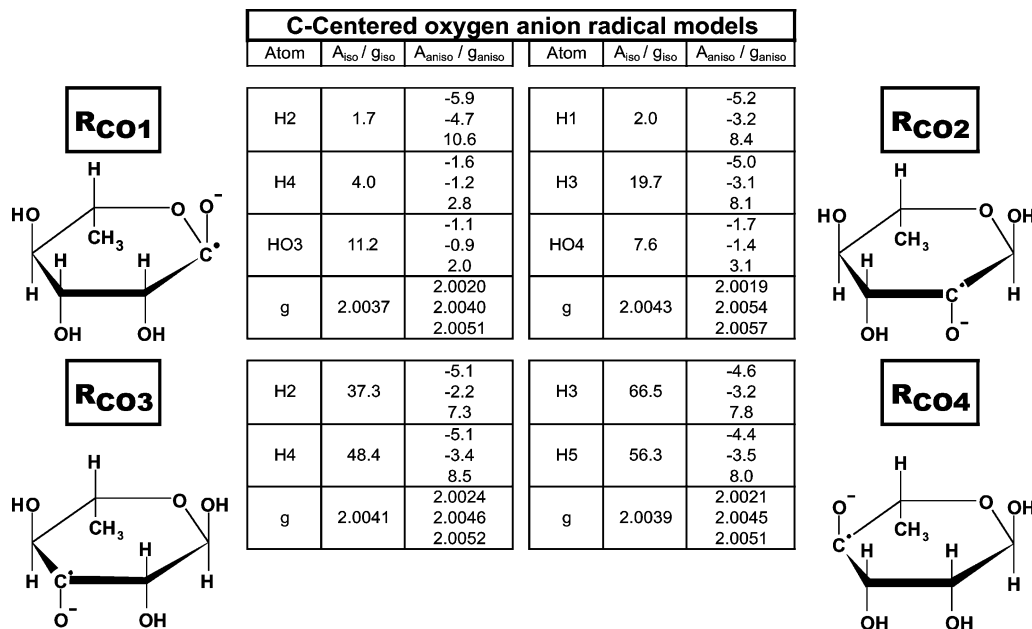


Figure 4. Overview of calculated g and hyperfine tensor values for carbon-centered oxygen anion radical models, obtained at the B3LYP-PM3-8/B3LYP-1 level. Hyperfine values in megahertz.

of these calculations it is highly unlikely that species II_{exp} would convert into a radical anion.

(iv) Finally, we have introduced four more radical models in search for the structure of the I_{exp} alkoxy species. Models $\text{R}_{\text{O}1}$ to $\text{R}_{\text{O}4}$ are derived from rhamnose by homolytic cleavage of an O–H bond. The calculated g and hyperfine tensors are presented in Figure 5, along with the corresponding structures. Most striking feature in these radicals is the relatively large anisotropy of the g tensor: principal values of up to 2.06 are obtained, which is typical for alkoxy radicals.²⁸ These tensors are sufficiently dissimilar, which makes it possible to distinguish between the models. For this reason, the eigenvectors have also been reported in Figure 5 as well as the angle deviations between experiment and theory: Ψ_{BB} with respect to experimental data from Budzinski and Box¹⁵ and Ψ_{SL} based on the data of Samskog and Lund.¹⁴ These deviations allow an easy assessment of the quality of the calculated principal directions. Model $\text{R}_{\text{O}4}$ is manifestly the best candidate for the alkoxy radical. Both Ψ_{BB} and Ψ_{SL} angles are less than 20° and the eigenvector corresponding to the maximum principal component even deviates by a mere 8° or 5° .

However, as already stated by Sagstuen et al.,¹⁶ there exists a discrepancy between the g tensor of Budzinski and Box and that of Samskog and Lund. Whereas the maximum anisotropic g component is about 2.04 in $\text{I}_{\text{exp,SL}}$, it is only 2.02 in $\text{I}_{\text{exp,BB}}$! In addition, the hyperfine coupling tensors for both species show substantial differences. Samskog and Lund report only two isotropic splittings—one large (≈ 120 MHz) and one intermediate (≈ 40 MHz)—but Budzinski and Box describe two intermediate couplings (54 and 67 MHz) among a series of smaller contributions (below 5 MHz). The calculated EPR data for radical model $\text{R}_{\text{O}4}$ are only in complete accordance with the results of Samskog and Lund. The maximum anisotropic g value is 2.04 and a 111 MHz coupling is found along with a 34 MHz hyperfine coupling constant. The residual H3 coupling is small enough to assume that it remained undetected in the experiment. Hence, our calculations confirm that the $\text{I}_{\text{exp,SL}}$ alkoxy radical has a structure according to $\text{R}_{\text{O}4}$.

Unfortunately, no other oxygen-centered radical model reproduces the $\text{I}_{\text{exp,BB}}$ results. $\text{R}_{\text{O}1}$ and $\text{R}_{\text{O}2}$ are both characterized

by a +200 MHz coupling, which is too large and the principal directions of the $\text{R}_{\text{O}3}$ g tensor deviate substantially. Under the assumption that our computational protocol is valid, one could then argue that the $\text{I}_{\text{exp,BB}}$ species could correspond to a hypothetical open-ring alkoxy structure, because such a model (whatever the structure) was a priori discarded in this work. Even so, it seems highly unlikely that such a species could occur, especially when taking into account that sample irradiation in the measurements of Budzinski and Box occurred at 4.2 K! Hence, it would be irrational to assume that elaborate ring opening reactions would take place at that temperature, whereas just the $\text{R}_{\text{O}4}$ structure was observed at 77 K by Samskog and Lund. Therefore, one can only conclude that the structure for the $\text{I}_{\text{exp,BB}}$ species cannot be assigned in the scope of the current computational model.

Based on preliminary, exploratory calculations on the $\text{R}_{\text{O}4}$ model, in which the dissociated HO4 proton was reintroduced in the cluster, it seems possible that the $\text{I}_{\text{exp,BB}}$ species is a precursor for the $\text{I}_{\text{exp,SL}}$ alkoxy radical. The existence of a primary reduction product was already hypothesized by Samskog and Lund. Also, such a $-\text{CHO}^{\cdot-}$ $-\text{H}^+$ species could explain the IBB-1 coupling assigned to the dissociated hydroxyl proton in ref 15. However, this assumption remains highly speculative and awaits confirmation, either from experiment or from more advanced computational methods.

4. Quantitative Analysis and Discussion

Based on the computationally less demanding B3LYP-PM3-8/B3LYP-1 protocol, it was possible to assign models to nearly all radical species that were identified in the EPR experiments. This assignment was mostly based on a qualitative comparison between calculated and experimental EPR parameters. In this section, we will enhance this agreement for each radical model by performing calculations at a more advanced level of theory. The radical structures obtained in the previous section were re-optimized using the B3LYP-8 methodology. EPR calculations on these geometries were done adopting the B3LYP-8 level for the hyperfine tensors and B3LYP-1 for the g tensors, as outlined in the computational details. The resulting spectroscopic properties are listed in Figure 6 along with an overview of the proposed

O-Centered radical models							
Atom	$A_{\text{iso}} / g_{\text{iso}}$	$A_{\text{aniso}} / g_{\text{aniso}}$	Direction Cosines vs $\langle a^*bc \rangle$			Ψ_{BB}	Ψ_{SL}
R₀₁							
H1	203.5	-8.2 -3.6 11.8	-0.513 -0.064 0.856	-0.018 -0.996 -0.085	0.858 -0.059 0.510		
H2	-7.7	-7.2 -2.3 9.5	0.673 -0.293 0.679	0.080 0.942 0.327	0.736 0.166 -0.657		
H3	6.1	-5.6 -2.3 7.9	0.675 0.735 0.068	0.632 -0.623 0.462	-0.382 0.269 0.884		
HO3	4.5	-1.1 -0.7 1.8	0.153 0.987 0.049	0.882 -0.159 0.444	-0.446 0.025 0.895		
g	2.0142	2.0021 2.0097 2.0308	0.053 -0.795 -0.604	-0.295 0.566 -0.770	0.954 0.219 -0.205	37 21 42	62 38 48
R₀₂							
H2	237.4	-9.0 -2.8 11.8	-0.151 0.988 -0.042	-0.373 -0.018 0.928	-0.916 -0.155 -0.371		
H4	5.8	-5.8 -3.7 9.5	-0.198 -0.523 0.829	0.046 -0.850 -0.525	0.979 -0.066 0.193		
g	2.0233	2.0023 2.0092 2.0583	0.651 0.209 -0.730	-0.594 -0.458 -0.661	-0.473 0.864 -0.174	96 21 38	61 67 44
R₀₃							
H2	13.7	-2.8 -2.3 5.1	0.944 0.017 0.328	0.292 0.417 -0.861	-0.151 0.909 0.389		
H3	96.7	-6.5 -3.8 10.4	0.416 0.442 0.795	-0.599 -0.525 0.605	-0.685 0.728 -0.047		
H4	-5.8	-9.2 -0.8 10.0	0.542 0.834 0.105	0.639 -0.328 -0.696	0.546 -0.444 0.710		
H6a	7.5	-1.1 -0.4 1.6	0.810 0.374 -0.453	-0.302 0.927 0.224	0.503 -0.044 0.863		
g	2.0176	2.0022 2.0088 2.0418	-0.189 -0.862 0.470	-0.787 -0.153 -0.597	0.587 -0.483 -0.650	11 81 81	27 76 80
R₀₄							
H2	34.0	-2.6 -0.3 2.9	0.686 0.391 0.613	-0.544 -0.283 0.790	-0.482 0.876 -0.019		
H3	-7.1	-9.5 -1.4 10.9	-0.227 0.967 -0.118	0.150 0.155 0.977	0.962 0.204 -0.180		
H4	110.8	-6.9 -4.3 11.2	0.419 -0.190 0.888	0.875 0.344 -0.340	-0.241 0.920 0.310		
g	2.0182	2.0022 2.0090 2.0433	-0.217 -0.718 -0.662	-0.885 0.431 -0.178	0.413 0.547 -0.728	18 19 8	18 19 5

Figure 5. Full g and hyperfine tensors for alkoxy radical models, calculated at the B3LYP-PM3-8/B3LYP-1 level of theory. Hyperfine values are in megahertz. Angle deviations Ψ_{BB} and Ψ_{SL} are in degrees.

radical models. Full hyperfine and g tensors are given and the corresponding eigenvectors are compared with their experimental counterparts (if available) with the aid of the Ψ angle deviation (in degrees).

Radical Species $\text{I}_{\text{exp,SL}}$. In the previous section, a structure according to model R_{04} was attributed to this radical species. Upon going to a higher level of theory, the calculated spectroscopic properties are not improving significantly with respect to the already good results of Figure 5. The Ψ angle deviations for the g tensor remain almost unchanged. The principal g tensor component, however, is now identical to the experimental value. At the B3LYP-8/B3LYP-8 level, H4 gives rise to a mere 100 MHz coupling which is somewhat smaller than the $\text{I}_{\text{SL-1}}$ splitting. The $\text{I}_{\text{SL-2}}$ coupling, on the other hand, is now perfectly reproduced by H2.

Radical Species II_{exp} and III_{exp} . At the B3LYP-PM3-8 level of theory, only one 18 MHz coupling (H2) was calculated for model R_{03} , whereas II_{exp} is characterized by two such splittings. The high-level calculations resolve this issue, as the HO3 hydroxyl proton now gives rise to a 12 MHz isotropic constant (Figure 6). This is mainly a structural effect, as the orientation of the O3–HO3 bond has changed (some 20°) with respect to the lone electron orbital containing the unpaired electron. The resulting redistribution of unpaired spin density has an appreciable impact on the hyperfine coupling constant. This effect is further illustrated in Figure 7, where the HO3 hyperfine splitting is plotted as a function of the HO3–O3–C3–C2 dihedral angle (all other structural parameters were constrained). The data in this plot is the result of several single molecule EPR calculations (B3LYP-1) starting from the B3LYP-8

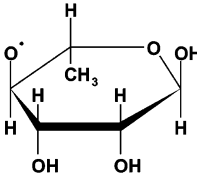
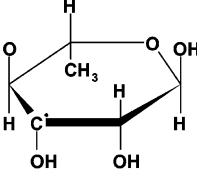
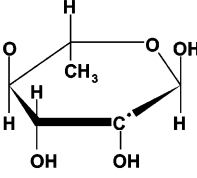
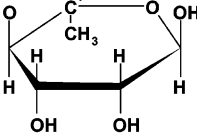
Atom	$A_{\text{iso}} / g_{\text{iso}}$	$A_{\text{aniso}} / g_{\text{aniso}}$	Direction Cosines vs $\langle a^*bc \rangle$			Ψ	Reference	
RO4 I_{exp},SL								
	H2	40.5	-3.0 -0.3 3.3	0.705 0.488 0.515	-0.521 -0.136 0.843	-0.481 0.862 -0.159	I _{SL} -2	
	H3	-6.1	-9.9 -0.8 10.7	-0.246 0.959 -0.142	0.154 0.184 0.971	0.957 0.217 -0.193		
	H4	100.4	-6.5 -4.4 11.0	0.470 -0.152 0.870	0.870 0.249 -0.426	-0.151 0.956 0.249		
g	2.0189	2.0022 2.0090 2.0456	-0.251 -0.690 -0.679	-0.885 0.448 -0.128	0.392 0.569 -0.723	19 19 3	I _{SL} -g	
RC3 II_{exp} III_{exp}								
	H2	14.6	-6.0 -3.6 9.6	-0.316 -0.657 0.684	-0.130 0.744 0.655	0.940 -0.118 0.320	II-2 / III-2	
	H4	87.4	-5.4 -2.2 7.6	-0.068 -0.966 0.251	0.399 0.204 0.894	0.915 -0.160 -0.371		12 15 5
	HO3	12.2	-12.1 -10.3 22.5	0.388 0.829 0.402	0.723 -0.544 0.426	-0.572 -0.126 0.811	II-3 / -	
	g	2.0031	2.0022 2.0032 2.0040	-0.592 -0.587 -0.552	0.787 -0.275 -0.552	-0.172 0.762 -0.625		41 31 27
RC2 IV_{exp}								
	H1	4.3	-6.0 -4.0 10.0	0.937 0.350 -0.010	-0.339 0.914 0.224	0.088 -0.207 0.974	15 15 2	IV-2
	H3	26.4	-6.3 -4.7 11.0	-0.462 0.407 0.788	0.563 0.821 -0.094	0.685 -0.400 0.609	5 3 4	
	H4	-3.3	-4.0 -1.4 5.4	-0.380 0.895 0.236	0.148 -0.193 0.970	0.913 0.403 -0.059	4 3 2	IV-4
	HO2	7.9	-11.6 -9.6 21.2	0.785 0.256 -0.565	0.567 -0.665 0.486	0.251 0.702 0.667	6 5 4	
	g	2.0032	2.0021 2.0031 2.0043	0.506 0.745 -0.436	0.837 -0.302 0.456	-0.208 0.595 0.776	17 15 8	IV-g
	RC5 V_{exp}							
	H4	90.6	-5.2 -2.1 7.3	0.681 0.488 -0.546	0.732 -0.468 0.495	0.013 0.737 0.676	V-1	
	H6a	15.7	-5.0 -4.3 9.2	0.280 0.788 -0.548	0.809 -0.501 -0.308	0.518 0.357 0.778		
	H6b	31.8	-5.2 -4.6 9.9	0.006 -0.594 0.805	0.114 0.800 0.589	0.993 -0.088 -0.073		
	H6c	109.4	-4.3 -2.6 6.9	0.504 0.805 0.313	0.246 -0.481 0.841	0.828 -0.347 -0.441	V-2	
	H6avg	52.3						
	g	2.0032	2.0021 2.0035 2.0039	-0.616 0.331 0.715	0.772 0.433 0.465	-0.156 0.839 -0.522		

Figure 6. Summary of calculated EPR data confirmed radical models. Hyperfine tensors determined with B3LYP-8/B3LYP-8 and g tensors with B3LYP-8/B3LYP-1. Hyperfine couplings in megahertz. Ψ angle deviations in degrees.

optimized geometry. The latter structure has a corresponding dihedral angle of 165.8°. It is clear from the figure that the HO3 isotropic coupling varies considerably, depending on its position with respect to the lone electron orbital (LEO). Maxima are noticed when the HO3–O3 bond is parallel with the direction of the LEO, indicated by dashed lines in the plot. In all, the RC₃ model structure determined from B3LYP-8 optimization is consistent with the II_{exp} radical species and near quantitative agreement between theory and experiment is obtained for all proton hyperfine couplings.

Furthermore, the large dependence of the HO3 coupling on its orientation might account for the disappearing hydroxyl proton splitting in the transformation of II_{exp} in III_{exp} with increasing temperature. In the undamaged crystal, the HO3 proton is held in position by one hydrogen bond with a nearby rhamnose molecule. However, as obtained from either B3LYP-PM3-8 or B3LYP-8 optimizations, this hydrogen bond is broken

in the radical structure. At 110 K then, it is possible that thermal motion for this degree of freedom levels out the HO3 hyperfine coupling. Alternatively, the radical might assume a geometry that corresponds to a local minimum, in which the orientation of the HO3 proton is altered. Although both assumptions are plausible, a definite validation can only be attained by performing more advanced calculations, in which temperature effects are taken into account. Therefore, the III_{exp} radical species is tentatively assigned a structure similar to the RC₃ model, with an altered orientation for the HO3 hydroxyl proton.

Full g and hyperfine tensors were determined for this radical species, as summarized in Table 1. In the work by Sagstuen et al.,¹⁶ the eigenvector corresponding to the maximum anisotropic hyperfine coupling (6.6 MHz) was found to be in close agreement with the crystallographic C3–H4 or C4–H3 directions. The direction cosines for these crystallographic vectors were also reported in the paper. However, a recalculation based

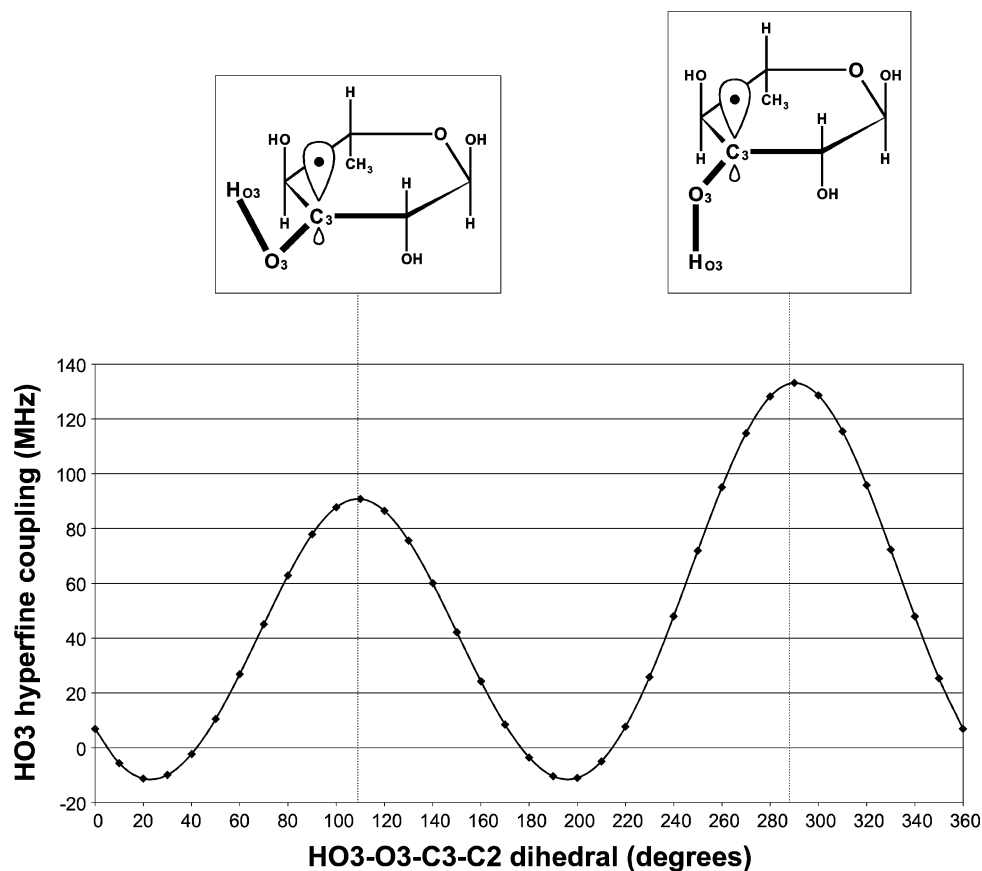


Figure 7. Isotropic hyperfine coupling constant for the HO3 hydroxyl proton in radical model R_{C_3} as a function of the HO3–O3–C3–C2 dihedral angle.

on the crystal structure as determined from neutron diffraction²² revealed a minor mistake in the signs of the $\langle a^* \rangle$ components of these directions. Hence, the principal directions for the hyperfine and g tensor were more than likely presented with a similar error. Consequently, all direction cosines for III_{exp} in Table 1 with respect to the $\langle a^* \rangle$ axis were subject to a sign reversal. If this correction is taken into account, the agreement between the B3LYP-8/B3LYP-8 hyperfine tensor for H4 in R_{C_3} and the III-1 tensor in III_{exp} becomes excellent. The isotropic constant is very slightly underestimated, but the direction cosines are in perfect agreement with the Ψ angle deviation never surpassing 15° . In addition, the H2 hyperfine value of 14.6 MHz is close to the experimental 16.8–19.6 MHz range. The g tensor, on the other hand, is not well reproduced, although it could be speculated that this spectroscopic property would also be influenced by thermal effects. Not only are the anisotropic components underestimated, but also the agreement between theoretical and experimental eigenvectors is poor, with a minimal angle deviation of 27° .

Radical Species IV_{exp}. From the EPR and ENDOR measurements by Sagstuen et al.,¹⁶ both (an)isotropic values and eigenvectors were determined for a lot of hyperfine tensors and the g tensor. This presents an extensive data set to evaluate the accuracies of the B3LYP-8/B3LYP-8 and B3LYP-8/B3LYP-1 methodologies in reproducing the hyperfine and g tensors, respectively. The calculated EPR data for model R_{C_2} , as listed in Figure 6, are quite spectacular. Not only are anisotropic hyperfine values perfectly reproduced, but also the theoretical isotropic couplings differ by 3 MHz at the most. Furthermore, even the corresponding direction cosines are very close to the measured ones, with Ψ angle deviations below the 20° threshold at all times. For the H3, H4 and HO2 hyperfine tensors the

accordance is even within 5° ! The g tensor is also quite accurate, especially when taking into account that this parameter was obtained at a much lower level of theory (B3LYP-1) due to computational restrictions. Although the maximum principal component is overestimated by some 700 ppm, the eigenvectors are close to their experimental counterparts.

For this radical species, the accuracy of the calculations is quite extraordinary. As a result, this comparison conclusively establishes that the computational protocol adopted in this work presents a valid approximation scheme to predict the EPR properties of radiation-induced carbohydrate radicals.

Radical Species V_{exp}. In the EPR experiment, only isotropic hyperfine couplings were obtained for this radical species. The agreement between theory (model R_{C_5}) and experiment remains satisfactory and is not altered by applying a higher level of theory (B3LYP-8/B3LYP-8). Calculated hyperfine and g tensors are reported in Figure 6 for the sake of completeness.

5. Energy Considerations

Up to now, radical structures were effectively assigned on the basis of their ability to reproduce experimental EPR properties. Additionally, it is of interest to mutually compare the binding energies of the radicals. In Table 2, the electronic energy differences are listed for all radicals in the B3LYP-PM3-8 scheme, relative to the energy of the R_{C_3} radical. In addition, the B3LYP-8 relative energies are reported for radicals R_{C_2} , R_{C_3} and R_{O_4} with respect to the R_{C_5} binding energy.

Concentrating first on the B3LYP-PM3-8 results, it is apparent that the energy is largely determined by the type of radical at hand. Neutral, carbon-centered radicals (R_{C_1} – R_{C_6}) differ 43 kJ/mol at most from the energy of the reference state,

TABLE 2: Energy Differences (kJ/mol) between Radicals, Relative to the Structure with Lowest Energy^a

	relative energies (kJ/mol)	
	B3LYP-PM3-9	B3LYP-8
R _{C1}	25.69	
R _{C2}	12.52	14.68
R _{C3}	0.00	2.09
R _{C4}	19.94	
R _{C5}	8.70	0.00
R _{C6}	43.04	
R _{O1}	53.59	
R _{O2}	69.69	
R _{O3}	105.53	
R _{O4}	50.95	54.63
R _{CO1}	1512.85	
R _{CO2}	1530.31	
R _{CO3}	1495.78	
R _{CO4}	1478.89	

^a At the B3LYP-PM3-8 level of theory this is R_{C3}, whereas radical R_{C5} has the lowest energy in the B3LYP-8 scheme. Only four structures were considered at the latter level of theory, due to the computational cost.

whereas the relative energies for oxygen-centered species (R_{O1}–R_{O4}) range from 50 to about 100 kJ/mol. Carbon-centered anion radicals (R_{CO1}–R_{CO4}) are significantly less stable, with energy differences as large as 1530 kJ/mol. The energetics of these radicals suggests that their occurrence in irradiated rhamnose is highly unlikely, as opposed to neutral radical species. The rejection of the anion radicals is therefore in complete agreement with the conclusions made on the basis of a comparative study of calculated and measured spectroscopic properties (section 3).

Figure 8 schematically compares the binding energies of the neutral radical species. Radical structure R_{O4}, which was attributed to the experimentally observed I_{exp,SL} radical, has the lowest relative energy from all alkoxy radicals. This could explain why none of the other alkoxy species was observed in EPR experiments, as radical R_{O4} is preferentially formed. However, some caution is required here. Because the radicals are the end result of irradiation of sugar molecules in the solid state, it is likely that, at some part along the radiation-induced decay route, excited states will play an essential role in the formation of the radicals. The determination of structures and energies for these excited-state species, embedded within the crystal lattice, is far beyond the scope of this work. Therefore, without any knowledge of these states, it is difficult to make an unquestionable interpretation of the observed radical occurrence in terms of their stabilities. Still, the ~50 kJ/mol energy difference of the alkoxy radical with the reference is qualitatively consistent with the fact that this species is only observed when irradiating rhamnose at low temperatures (e.g., 4–80 K). R_{O4} is clearly a transient radical that becomes “trapped” within the rhamnose matrix when not enough thermal degrees of freedom are available.

Also for the carbon-centered radical structures in Figure 8, those with lowest energy (i.e., R_{C2}, R_{C5} and R_{C3}) have been attributed to measured species (IV_{exp}, V_{exp} and II_{exp}/III_{exp} respectively). Again, the relative instability of the R_{C1}, R_{C4} and R_{C6} radicals is in accordance with the fact that they are not observed in EPR experiments.

Examining the B3LYP-8 energies, only minor changes are apparent with respect to the B3LYP-PM3-8 sequence. The most drastic change occurs for R_{C5}, which drops about 9 kJ/mol and becomes the new reference at the B3LYP-8 level of theory. Nevertheless, the calculated energy sequence of the radicals that

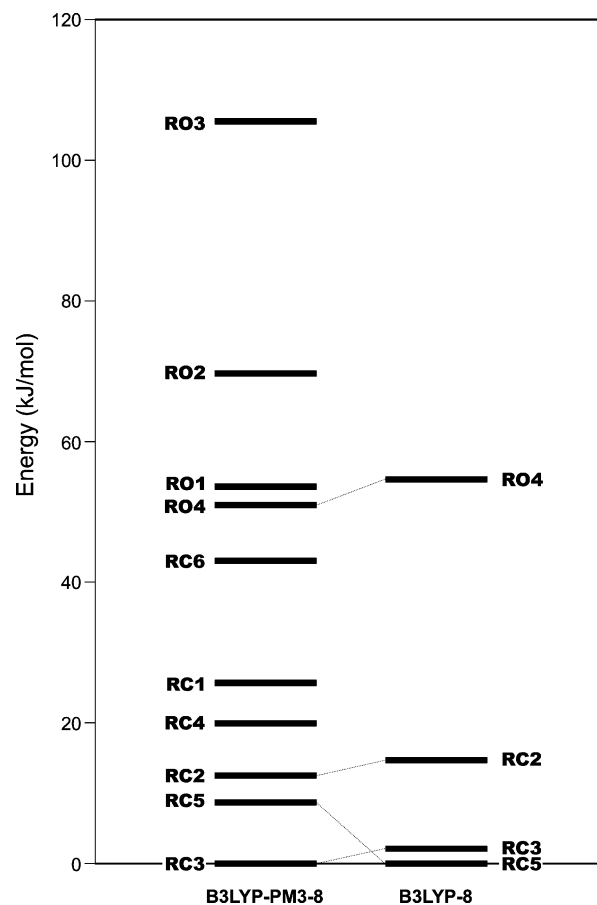


Figure 8. Schematic representation of relative energies for all neutral rhamnose radicals.

emerges from the calculations is quite satisfactory from a qualitative point of view: (neutral) carbon-centered radicals are more stable than the R_{O4} alkoxy, which is clearly a transient species.

6. Conclusions

With the aid of DFT calculations, a multitude of possible structures was examined to reproduce both *g* and hyperfine coupling tensors of radiation-induced radicals in α -L-rhamnose. For this purpose, a cluster approach was applied, in which all hydrogen bonds between the radical and its surroundings were taken into account. Intermolecular interactions were first treated at a semiempirical level of theory, which allowed a fast, initial assessment of the different radical models. From qualitative comparison of calculated EPR parameters with experimental data, four radical models were obtained for the five rhamnose species that were observed in measurements. Following this primary selection, the remaining radical models were treated at a high level of theory, which produced a near quantitative agreement with experiment.

On the basis of our calculations, radical models R_{C3}, R_{C2} and R_{C5} were found to reproduce the EPR properties of the observed species II_{exp}, IV_{exp} and V_{exp}, respectively. Because identical structures were suggested earlier from the EPR experiments, DFT methods have independently presented a validation for these models. In addition, these radicals had the lowest energy of all calculated structures, which might account for their occurrence in irradiated rhamnose. The R_{C3} hydroxyalkyl structure was also attributed to the carbon-centered III_{exp} radical, under the assumption that the orientation of the HO3–O3 hydroxyl group is slightly altered due to (most likely) thermal

effects. Contrary to the initial suggestion in the experiment, our calculations effectively rule out the occurrence of a carbon-centered oxygen anion radical for this species. The Samskog and Lund EPR measurements of the rhamnose alkoxy radical were well reproduced by the R_{O_4} radical model. As its energy was higher than that of carbon-centered radicals, our calculations corroborate the transient nature of the alkoxy radical, which can only be detected by irradiation and measurement at low temperatures. However, the current computational approach cannot account for the alkoxy species identified by Budzinski and Box at a much lower temperature, even though these researchers proposed a structure similar to R_{O_4} . Hence, a conclusive validation for this radical model will require more advanced theoretical models, in which, presumably, the dissociated HO4 proton has to be taken into account.

The B3LYP-8/B3LYP-8 methodology for the determination of hyperfine coupling tensors provides a sometimes small, but often appreciable improvement over the B3LYP-PM3-8/B3LYP-1 method. Besides the apparent superior description of radical geometries, the EPR calculation in the former approach benefits substantially from the treatment of the radical in the presence of its molecular environment. This purely electronic effect is therefore not to be undervalued and clearly indicates that the results of a single molecule EPR calculation must always be analyzed with caution. Nevertheless, the B3LYP-PM3-8/B3LYP-1 method usually remains accurate enough to allow a qualitative assessment of radical models.

In addition, g tensors were determined for all radical models within the DFT framework. Due to the associated computational cost, calculations were restricted to a single molecule approach for this property only. For carbon-centered radicals, the g tensor is not a suitable probe to evaluate a radical model, as it is largely isotropic and virtually impartial to (relatively small) changes in radical geometry. The rather large g tensor anisotropy in alkoxy radicals, on the other hand, is quite sensitive to structural alterations. Hence, DFT calculations of the g tensor for these radical species can be useful to assess the validity of a proposed radical model and can quantitatively reproduce the experimental tensor.

Acknowledgment. This work is supported by the Fund for Scientific Research—Flanders (FWO) and the Research Board of the Ghent University.

Supporting Information Available: g and hyperfine tensor values and geometric parameters. This material is available free of charge via the Internet at <http://pubs.acs.org>.

References and Notes

- Fattibene, P.; Duckworth, T. L.; Desrosiers, M. F. *Appl. Radiat. Isotopes* **1996**, *47*, 1375. Nakajima, T.; Otsuki, T.; Hara, H.; Nishiwaki, Y.; Matsuoka, M. *Radiat. Prot. Dosim.* **1990**, *34*, 303. Tchen, A.; Greenstock, C. L.; Trivedi, A. *Radiat. Prot. Dosim.* **1993**, *46*, 119. Nakagawa, K.; Nishio, T. *Radiat. Res.* **2000**, *153*, 835. Yordanov, N. D.; Georgieva, E. *Spectrochim. Acta A* **2004**, *60*, 1307. Da Costa, Z. M.; Pontuschka, W. M.; Campos, L. L. *Appl. Radiat. Isotopes* **2005**, *62*, 331.
- Ikeya, M. *New applications of electron spin resonance: dating, dosimetry and microscopy*; World Scientific: Singapore, 1993. Fattibene, P. *Appl. Radiat. Isot.* **1996**, *47*, 1375. Esteves, M. P.; Andrade, M. E.; Empis, J. *Radiat. Phys. Chem.* **1999**, *55*, 737. Da Costa, Z. M.; Pontuschka, W. M.; Campos, L. L. *Appl. Radiat. Isot.* **2005**, *62*, 331.
- Atherton, N. M. *Principles of Electron Spin Resonance*; Ellis Horwood, Prentice Hall: New York, 1993. Weil, J. A.; Bolton, J. R.; Wertz, J. E. *Electron Paramagnetic Resonance: Elementary Theory and Practical Applications*; Wiley-Interscience: New York, 1994.
- Madden, K. P.; Bernhard, W. A. *J. Phys. Chem.* **1982**, *86*, 4033. Madden, K. P.; Bernhard, W. A. *J. Phys. Chem.* **1979**, *83*, 2643.
- Vanhaelewyn, G.; Lahorte, P.; De Proft, F.; Mondelaers, W.; Geerlings, P.; Callens, F. *Phys. Chem. Chem. Phys.* **2001**, *3*, 1729.
- Vanhaelewyn, G.; Jansen, B.; Pauwels, E.; Sagstuen, E.; Waroquier, M.; Callens, F. *J. Phys. Chem. A* **2004**, *108*, 3308.
- Gräslund, A.; Löfroth, G. *Acta Chem. Scand. B* **1975**, *29*, 475. Sagstuen, E.; Lund, A.; Awadelkarim, O.; Lindgren, M.; Westerling, J. *J. Phys. Chem.* **1986**, *90*, 5584. Vanhaelewyn, G.; Sadlo, J.; Callens, F.; Mondelaers, W.; De Frenne, D.; Matthys, P. *Appl. Radiat. Isotopes* **2000**, *52*, 1221.
- Close, D. M. *Radiat. Res.* **1997**, *147*, 663. Shukla, L. I.; Pazdro, R.; Becker, D.; Sevilla, M. D. *Radiat. Res.* **2005**, *163*, 591.
- Box, H. C.; Budzinski, E. E.; Freund, H. G. *J. Chem. Phys.* **1978**, *69*, 1309.
- Budzinski, E. E.; Potter, W. R.; Potienko, G.; Box, H. C. *J. Chem. Phys.* **1979**, *70*, 5040.
- Box, H. C.; Budzinski, E. E.; Freund, H. G. *J. Chem. Phys.* **1990**, *121*, 262.
- Samskog, P. O.; Lund, A.; Nilsson, G.; Symons, M. C. R. *J. Chem. Phys.* **1980**, *73*, 4862.
- Samskog, P. O.; Kispert, L. D.; Lund, A. *J. Chem. Phys.* **1983**, *79*, 635.
- Samskog, P. O.; Lund, A. *Chem. Phys. Lett.* **1980**, *75*, 525.
- Budzinski, E. E.; Box, H. C. *J. Chem. Phys.* **1985**, *82*, 3487.
- Sagstuen, E.; Lindgren, M.; Lund, A. *Radiat. Res.* **1991**, *128*, 235.
- For an example of a reference work, see: Parr, R. G.; Yang, W. *Density-Functional Theory of Atoms and Molecules*; Oxford University Press: New York, 1989.
- Guerra, M. *Phys. Chem. Chem. Phys.* **2001**, *3*, 3792. Parr, K. D.; Wetmore, S. D. *Chem. Phys. Lett.* **2004**, *389*, 75. Wetmore, S. D.; Boyd, R. J.; Eriksson, L. A. *J. Phys. Chem. B* **1998**, *102*, 7674. Pauwels, E.; Lahorte, P.; Vanhaelewyn, G.; Callens, F.; De Proft, F.; Geerlings, P.; Waroquier, M. *J. Phys. Chem. A* **2002**, *106*, 12340.
- Pauwels, E.; Van Speybroeck, V.; Lahorte, P.; Waroquier, M. *J. Phys. Chem. A* **2001**, *105*, 8794. Pauwels, E.; Van Speybroeck, V.; Waroquier, M. *Int. J. Quantum Chem.* **2003**, *91*, 511.
- Pauwels, E.; Van Speybroeck, V.; Waroquier, M. *J. Phys. Chem. A* **2004**, *108*, 11321.
- Pauwels, E.; Van Speybroeck, V.; Waroquier, M. *Spectrochim. Acta, Part A* **2006**, *63*, 795.
- Takagi, S.; Jeffrey, G. A. *Acta Crystallogr. B* **1978**, *34*, 2551.
- Maseras, F.; Morokuma, K. *Comput. Chem.* **1995**, *16*, 1170. Svensson, M.; Humbel, S.; Froese, R. D. J.; Matsubara, T.; Sieber, S.; Morokuma, K. *J. Phys. Chem.* **1996**, *100*, 19357. Humbel, S.; Sieber, S.; Morokuma, K. *J. Chem. Phys.* **1996**, *105*, 1959. Matsubara, T.; Sieber, S.; Morokuma, K. *Int. J. Quantum Chem.* **1996**, *60*, 1101. Dapprich, S.; Komaromi, I.; Byun, K. S.; Morokuma, K.; Frisch, M. J. *J. Mol. Struct. (THEOCHEM)* **1999**, *462*, 1.
- Becke, A. D. *J. Chem. Phys.* **1996**, *104*, 1040.
- Krishnan, R.; Binkley, J. S.; Seeger, R.; Pople, J. A. *J. Chem. Phys.* **1980**, *72*, 650. McLean, A. D.; Chandler, G. S. *J. Chem. Phys.* **1980**, *72*, 5639.
- Stewart, J. J. P. *J. Comput. Chem.* **1989**, *10*, 209. Stewart, J. J. P. *J. Comput. Chem.* **1989**, *10*, 221.
- Vanhaelewyn, G.; Pauwels, E.; Callens, F.; Waroquier, M.; Sagstuen, E.; Matthys, P. *J. Phys. Chem. A* **2006**, *110*, 2147.
- Box, H. C.; Budzinski, E. E.; Freund, H. G. *J. Chem. Phys.* **1984**, *81*, 4898.